Advanced Materials Technology Insertion

Lawrence W. Hunter, Donald D. Duncan, Frank F. Mark, James S. O'Connor, and James W. White

This article highlights the accomplishments of an independent research and development effort undertaken in response to the increasing importance of advanced materials to the Laboratory's future work.

INTRODUCTION

The use of advanced structural materials in missiles, satellites, ships, and submarines—all systems of importance to the Laboratory—is rapidly increasing. Advanced materials offer lighter weight, higher strength, and improved resistance to heat and chemical attack; some lend themselves as agents for certain active control functions (by dimensional or viscosity change). The payoff is improved performance of systems applications, including higher thrust-to-weight ratios for aircraft and rockets and improved resistance of satellites to laser and nuclear radiation.

The Advanced Materials Technology Insertion project was launched to advance APL's capabilities to model, design, fabricate, and test prototype advanced materials/structures to enhance performance throughout their life cycle. The project was active as a Laboratory-wide thrust area and was supported by independent research and development funds from January 1990 through September 1994. To achieve diversification, the project (coordinated by L. W. Hunter) comprised a series of small, mainly independent tasks whose specific objectives were modest. Each one, however, made a unique contribution. All eight tasks focused on structural materials rather than optical and electronic materials, and addressed the interactions between the materials and their environment. Completed tasks and contributors are listed in the boxed insert.

Task 1 demonstrated a special technique needed to fabricate vessels for use in deep sea environments, where the pressure tends to collapse the vessel. The task successfully showed approaches for fabricating the especially difficult geometries of intersecting cylinders and fittings.

Task 2 focused on the fabrication of copper–graphite radiation shields to protect spacecraft electronic components from nuclear and ionizing radiation. The shields have favorable structural characteristics, meet rigorous outgassing requirements for space qualification, are lighter than conventional copper metallic shields, and can be customized for an anticipated radiation environment.

In parallel, Task 3 enhanced our in-house capability in heat pipe applications. Heat pipes carry heat rapidly from a hot to a cool region without the need for mechanical pumping of the coolant. Successful thermal management results in survivability of materials, increased strength, reduced corrosion, and reduced thermal stresses (as structures are isothermalized).

In Task 4, a trainable, quick diagnostic system was developed to advise operators performing nondestructive inspections of aircraft, new ship structures, and other critical composite structures. Neural network algorithms were taught to recognize individual, interlaminar flaw structures from ultrasonic scans. This

COMPLETED TASKS IN THE ADVANCED MATERIALS TECHNOLOGY INSERTION PROJECT

Task titles are followed by the names of the principal investigators (PIs) and main contributors (in alphabetic order; affiliations are also noted when other than APL).

1. Composite Pressure Vessels—Intersecting Cylinders with Fittings: P. J. Biermann (PI), S. Cooper, and G. Dailey
2. Reduced-Weight Satellite Radiation Shields from Composites: J. J. Suter (PI), J. C. Poret, and M. Rosen (JHU, Dept. of Materials Science and Engineering)
3. Extending Materials Performance in Hypersonic Platforms: F. G. Arcella (PI), S. Corda, M. A. Friedman, L. W. Hunter, and J. B. Kouroupis
4. New Advisory Tools for On-Line/In-Field Inspection of Composites: F. G. Arcella (PI), P. J. Biermann, L. Brown (David Taylor Research Center), M. A. Friedman, P. C. Lebowitz, and R. W. Newman
5. New Methods for Testing Materials Exposed to Heat and Oxidation: L. W. Hunter (PI), D. A. Carpenter, M. A. Friedman, J. R. Kuttler, F. F. Mark, R. M. Sova, and M. E. Thomas
6. Noncontact Strain Measurements: D. D. Duncan (PI), L. W. Hunter, S. J. Kirkpatrick, and F. F. Mark
7. Novel Smart Materials and Structures Made with Electrorheological Fluids: L. W. Hunter (PI, FY91–93), F. F. Mark (PI, FY94), F. G. Arcella, P. J. Biermann, J. Coulter (Lehigh University), M. D. Donohue (JHU, Dept. of Chemical Engineering), M. R. Feinstein, J. R. Kime, D. A. Kitchin, D. R. Kuespert (JHU, Dept. of Chemcial Engineering), J. S. O'Connor, and B. Platte
8. Nonmetallic Motor Liner Materials: J. W. White (PI) and P. J. Biermann

activity progressed to on-line diagnostics and control work in which the patterns of real-time sensor signatures were analyzed with neural network feature extractors and expert systems in order to perform process control and to support condition-based (as opposed to calendar-based) maintenance.

Highlights of the remaining tasks are described in more detail in the following sections. Readers interested in other recent Laboratory accomplishments in materials research and applications (covering structural, optical, and electronic materials) are referred to volumes 13(3) and 14(1) of the *Johns Hopkins APL Technical Digest*.

NEW METHODS FOR TESTING MATERIALS EXPOSED TO HEAT AND OXIDATION

This task focused on the fabrication of a novel apparatus to evaluate the performance of materials at ultrahigh temperatures in the presence of oxygen. New materials that can resist heat and oxidation are needed in future high-speed vehicles. The materials considered here resist heat and oxidation by forming an adherent solid-oxide coating (passive oxidation). The rate of formation and the adherence properties of the oxide determine the lifetime and maximum speed of the vehicle.

The original motivation for this task was the need to develop materials for the combustor liner of a new ramjet concept being designed by the Laboratory for use onboard ships.[1] Ramjets carry fuel but no oxidizer, and must be boosted to a speed at which the air intake is adequate for net thrust. However, ramjets have two advantages over rockets for shipboard use: (1) a greater powered range and (2) the option to throttle the engine and retarget the missile in flight. For a given launch tube volume, a ramjet flies a flat trajectory, which takes it farther and faster than a rocket, whose ballistic trajectory can be 250 mi high for a 600-mi range.

Predicted combustion temperatures for planned missions exceed 3000 K, so carbon becomes the candidate material for the combustor walls (the strength of carbon materials, unlike metals, can increase as temperature rises). However, engine cycle analyses predict that optimum thrust will occur with excess air, creating a combustor environment in which carbon burns. A few materials (namely ceramic oxides) can resist oxidation at 3000 K, but they unfortunately react with carbon and cannot form a bond.

Several organizations participated in the search for ramjet combustor liner materials,[2] mainly under sponsorship of the White Oak Naval Surface Weapons Center (so called at the time). In addition, the Laboratory's Milton S. Eisenhower Research Center solved several basic research problems.[3] The most promising idea was to coat the carbon with a ceramic carbide.[4,5] Arc heater tests[6] showed that hafnium carbide, in particular, formed a protective oxide scale at 3000 K on the side away from the carbon. In addition, a reasonable carbide thickness could be expected to protect the underlying carbon for one 10-min ramjet flight before the carbide was completely oxidized and attack on the carbon began.

The laser heating apparatus fabricated in this task (Fig. 1) enables similar candidate materials to be screened and evaluated at temperatures up to 3000 K. Specifically, it allows oxidation measurements to be made with better control of experimental variables than more expensive arc heaters, vitiated air heaters, and other laser facilities. The heat source is the Laboratory's CO_2 laser, which can be varied up to 570 W continuous wave. The apparatus uses a self-aligned optical bench containing beam-integration optics and a pyrometer tied to an automatic data acquisition system. The delivered heat flux is uniform over a 9 × 9 mm square, large enough to eliminate lateral heat conduction effects at the center. Pyrometer measurements agree with readings from imbedded

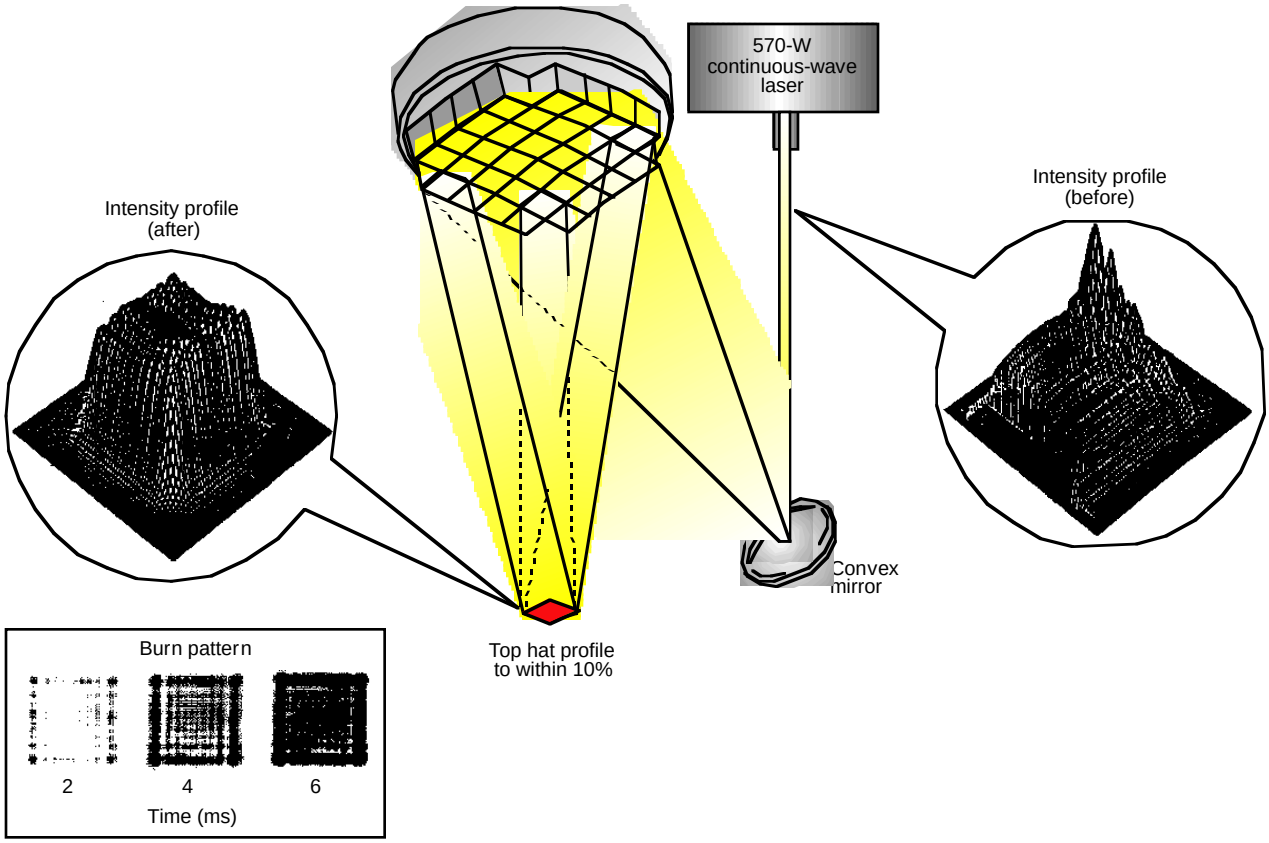

Figure 1. APL's laser heating capability. The delivered heat flux reaches 700 W/cm^2 = 4.3 BTU/in^2·s = 625 BTU/ft^2·s; blackbody temperature reaches 3260 K (≈5440°F). The apparatus has the following advantages: uniform heat flux over a 9 × 9 mm area; accurate temperature control; long exposure times; low background thermal reradiation, which permits speckle strain measurement at higher temperatures; and noncontact heating.

thermocouples. The atmosphere control box (Fig. 2) also accommodates the collection of laser speckle for simultaneous thermal expansion or creep measurements by a new technique described in what follows.

As a demonstration, hafnium carbide was oxidized in ambient air in the apparatus. The specimen was identical to those exposed for 10 min in earlier arc heater tests,[6] but here the focus was on its initial response.[7,8] Interestingly, a new phase was detected, and the total depth of oxidation exceeded predictions based on a model that agreed with the longer arc heater tests. The chemical composition of the new phase and the discrepancy in the depth of oxidation remain unresolved.

Related work on the theory addressed temperature gradients with variable thermal conductivity[9–12] and the development of a novel and more efficient algorithm for calculating the internal temperature distribution of an ablating material.[13] The algorithm applies to materials that gasify at a known temperature or melt when the liquid is immediately removed. The challenge here is that the location of the exposed surface is unknown in advance. The approach developed makes possible a single integration grid, which does not need to adapt to the changing surface location. All the nonlinearities of the problem are combined into a single functional relationship between the enthalpy and a generalized temperature.

NONCONTACT STRAIN MEASUREMENTS

The adherence of high-temperature protective coatings is often tied to their thermal expansion, strain, and creep behavior; a good match with the substrate is needed to avoid crack formation and disbonding, especially under thermal cycling. The same properties are important for fibers and (single-crystal) whiskers used to strengthen composite materials. Hence, the expansion, strain, and creep properties of candidate advanced materials must be screened. The difficulty in the ramjet application discussed previously is that the data are needed at temperatures as high as 3000 K, so any clamps must be well outside the hot zone.

An older approach was to scratch two marks on the surface of the test material and track the changing diffraction pattern produced as the material's dimensions changed. One disadvantage of such an approach

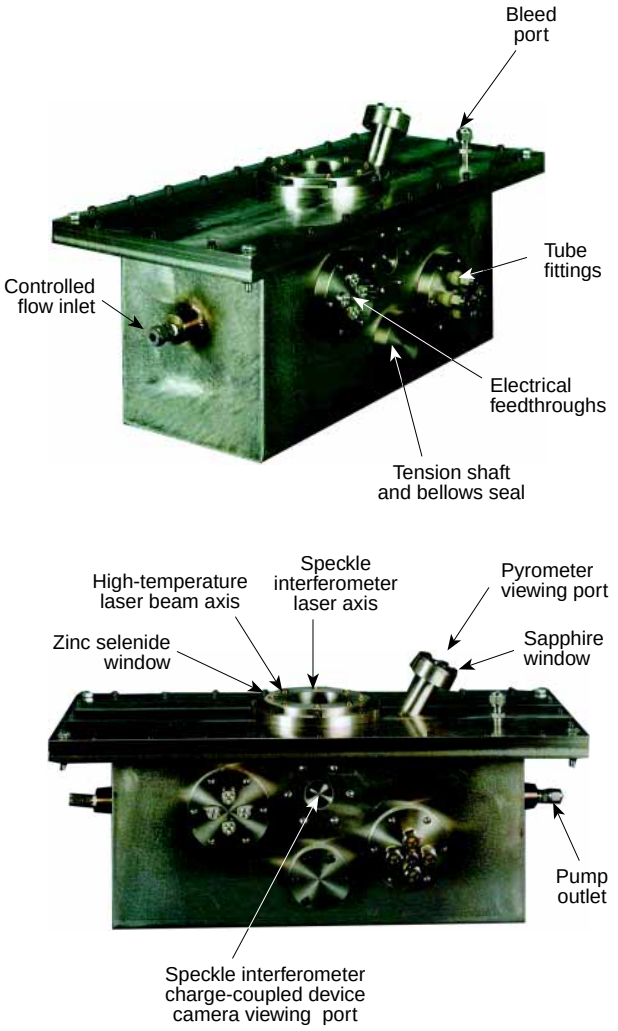

Figure 2. This high-temperature controlled atmosphere chamber provides control of composition and pressure and accommodates laser heating; noncontact measurement of creep, strain, and thermal expansion; and surface temperature pyrometry. This stainless steel chamber measures 6 × 7 × 15 in.

is that the scratches can initiate cracks. Another is that the measurements apply at only one scale, namely, the distance between the scratches. The approach we prefer tracks the motion of the "speckle" interference pattern produced when an incident laser beam interferes with the microscopic surface roughness comparable in size to the wavelength of the light. The pattern would be understandably difficult to model, but its motion is readily measured and is simply related to the material's surface motion, which is of interest. We proved that one speckle measurement is equivalent to many measurements using pairs of scratches at different spacings; thus, the statistics of our measurement are greatly improved. In addition, we developed a novel data processing method that is insensitive to vibrations and turbulence, fast, and more accurate. Other advantages of our technique are its compact design and modest resolution requirements. The speckle pattern is observed with a linear array detector.

Our most recent work is on the measurement of strain rates in fibers typically used to reinforce composite materials. The strains of interest are on the order of tens of parts per million and less. Because the requisite forces on these fibers are small (fibers are typically on the order of 10 to 100 mm in diameter), we designed and constructed our own microtensile test machine (Fig. 3). It is made of aluminum and stainless steel, with a micrometer head at one end and a piezoelectric transducer (PZT) at the other. The fiber is clamped between two collet-type chucks, one in contact with the micrometer head and the other rigidly attached to the load cell. The load cell in turn is attached to the PZT. The load cell is a tension/compression device with a maximum load range of 1 kg. Its output is first input to a full bridge network and then to a PC. The PZT is equipped with a displacement sensor, allowing it to be run in a closed-loop configuration with a maximum excursion of 40 μm, and maximum compressive and tensile forces of 100 and 10 N, respectively. In an actual experiment, a fiber is secured in the collets, and the micrometer head is backed off to allow preloading of the specimen. A sawtoothed voltage waveform is then applied to the PZT, causing a periodic strain variation in the fiber.

Our measurement concept is as follows: The object under tensile stress is illuminated sequentially with a collimated laser beam at off-axis angles of $\pm\theta_s$ and observed normally with a linear charge-coupled device array camera; the illuminated portion of the specimen constitutes the gauge size.

Yamaguchi[14] has shown that the speckle motion observed at angle θ_0 for illumination at angle θ_s is given by

$$\delta x(\theta_0, \theta_s) = a_x\left(\frac{L_0 \cos^2\theta_s}{L_s \cos\theta_0} + \cos\theta_0\right) - a_z\left(\frac{L_0 \cos\theta_s \sin\theta_s}{L_s \cos\theta_0} + \sin\theta_0\right) - L_0\left[\epsilon_{xx}\left(\frac{\sin\theta_s}{\cos\theta_0} + \tan\theta_0\right) - \Omega_y\left(\frac{\cos\theta_s}{\cos\theta_0} + 1\right)\right], \quad (1)$$

where

a_x = an in-plane motion,
a_z = an out-of-plane motion,
ϵ_{xx} = the linear strain in the plane of the laser beam and detector,
Ω_y = a rotation about the axis perpendicular to the measurement plane,

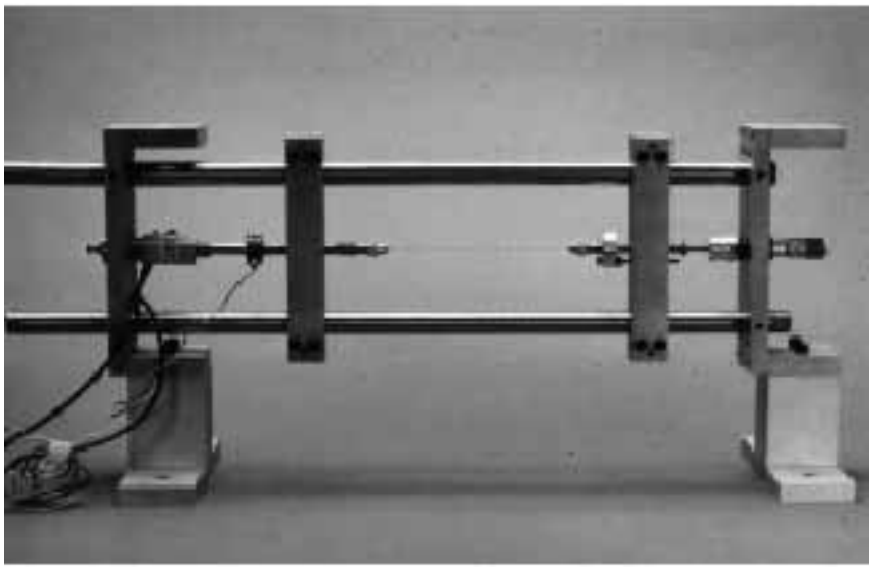

Figure 3. Microtensile test machine.

L_0 = the observation distance, and
L_s = the source distance.

By observing normally ($\theta_0 = 0$), using collimated laser beams ($L_s \rightarrow \infty$) and subtracting the speckle movements observed for two equal but opposite source angles, we arrive at the formula for differential speckle motion (before and after stress):

$$\delta A_x \equiv \delta x(0, \theta_s) - \delta x(0, -\theta_s) = -2L_0 \epsilon_{xx} \sin \theta_s \,. \qquad (2)$$

This result suggests that, by measuring the differential speckle motion, one can infer the strain, ϵ_{xx}.

Figure 4 is a schematic of the measurement configuration. The entire experiment is managed by an IBM PC. The camera is controlled by means of a plug-in card on the computer bus. Integration time, sample rate, and data acquisition are all adjustable in software. Strain data from the load cell are recorded using a plug-in analog–digital card. This same card produces (under software control) the square-wave voltages used to trigger the shutters and the camera.

As suggested previously, the crux of the problem is to determine the speckle pattern shifts resulting from the strain. Traditionally,[15,16] these shifts have been determined by calculating the cross correlation between the two patterns and pinpointing the location of the peak value. We have taken an entirely different approach that uses what we call a speckle history.[17,18]

Figure 5 shows a typical speckle pattern as recorded by a linear array camera. When a sequence of speckle patterns such as this is combined in an array, one obtains a spatiotemporal history of the speckle patterns. A gray-level display of such a speckle history, shown in Fig. 6, is a sequential record of one-dimensional speckle patterns such that the spatial dimension is horizontal and the temporal axis is vertical. For this measurement, the object underwent a slow linear strain from −10 to +10 $\mu\epsilon$. Here, ϵ signifies "strain," so that $\mu\epsilon$ denotes microstrain, or parts per million. In this display, one perceives the slow movement of the speckle pattern.

The information we seek is the time rate of speckle pattern movement, which is reflected in the tilt of the corrugated structure. A convenient means of extracting an estimate of this tilt is to perform a two-dimensional fast Fourier transform (FFT). Figure 7 shows the result of such an operation. In this frequency domain, the horizontal axis is spatial frequency and the vertical axis is temporal frequency. Zero frequency ("DC") is in the center. The bright line passing through zero frequency is perpendicular to the corrugated structure shown in Fig. 6. Its slope, therefore, is simply the time rate of speckle pattern shift. By taking the difference of these slopes as seen for the two illumination angles, the (time rate

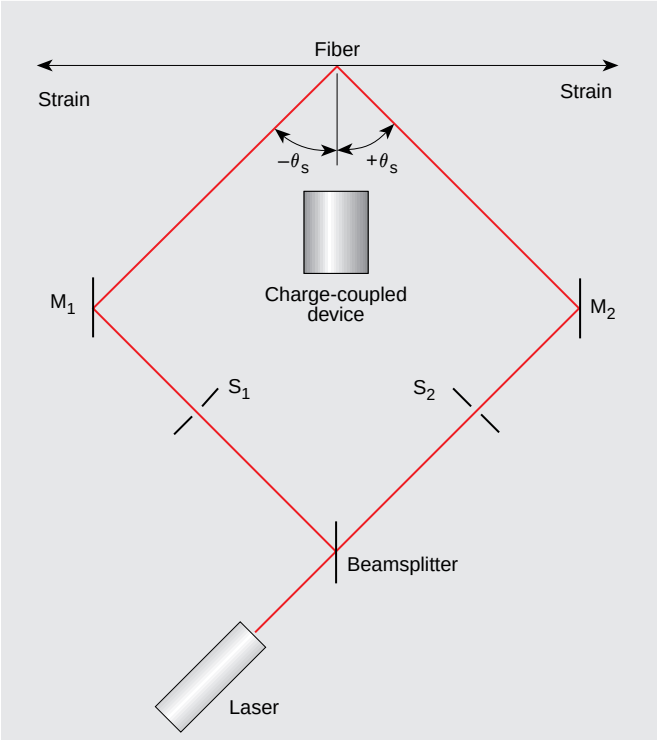

Figure 4. Measurement configuration. S_1 and S_2 are shutters, M_1 and M_2 are mirrors, and θ_s denotes the off-axis angle.

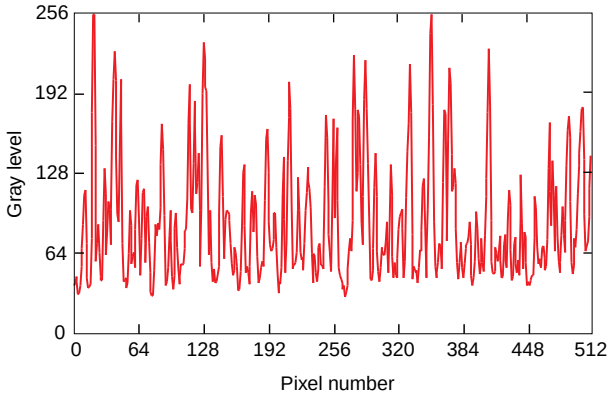

Figure 5. Typical speckle pattern.

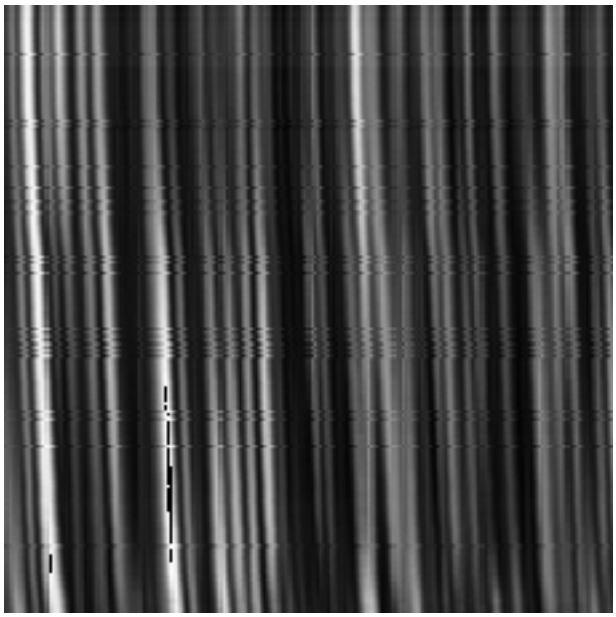

Figure 6. Display of speckle history.

of) strain can be inferred through Eq. 2. Specifically, we use the time derivative of that equation:

$$\delta\dot{A}_x \equiv \delta\dot{x}(0,\theta_s) - \delta\dot{x}(0,\theta_s) = -2L_0\dot{\epsilon}_{xx}\sin\theta_s\,. \qquad (3)$$

Inversion of this equation yields the estimate for the strain rate:

$$\dot{\epsilon}_{xx} = \frac{(m_2 - m_1)}{2L_0\sin\theta_s}\,, \qquad (4)$$

where m_1 and m_2 represent the slopes as calculated for the two illumination angles.

In principle, the spectral transformations can be performed using an FFT. However, we have had better results using an FFT in the spatial dimension and a parametric estimator[19] in the temporal dimension.

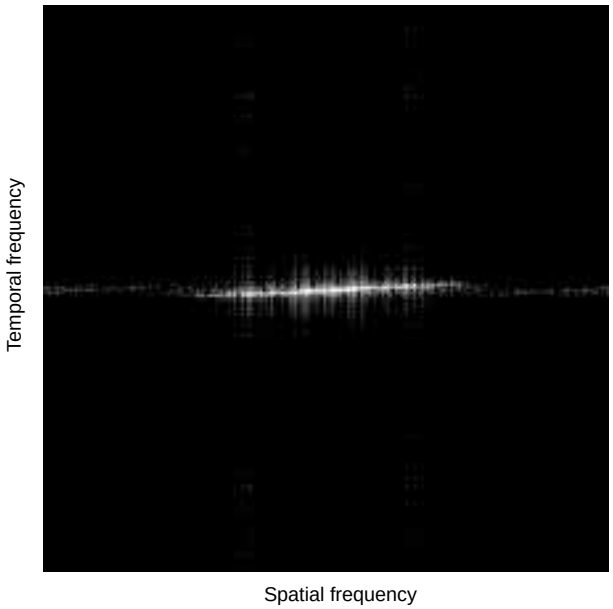

Figure 7. "Focused" speckle history.

Specifically, we use an autoregressive estimator (modified covariance method) on 10 to 20 records with 3 to 5 poles. One characteristic of such parametric estimators is their ability to incorporate *a priori* knowledge about the form of the computed spectrum. In our case, we know that the focused speckle history will consist of a well-localized bright line running through the DC point. In addition, parametric models such as these tend to produce very "spiky" spectra, thus allowing good resolution with short data records. This characteristic, in turn, helps us analyze signals that are not stationary, such as those observed when the speckle patterns, for sufficiently large strains, become decorrelated.

This approach to evaluating speckle translation is a straightforward generalization of the method of Sharpe[20] (see the boxed insert, Laser Speckle). In this technique, a hardness tester is used to produce a pair of indentations in the material. Illumination by a coherent source then produces Young's fringes (see boxed insert on same), which are monitored with a pair of detectors. As in our approach, the differential configuration allows the subtraction of rigid body motions.

Our speckle history approach to processing Sharpe's data (from each detector) would produce a single pair of bright spots, symmetrically arrayed about zero frequency, in the frequency plane. The slope of the line connecting these two bright spots is the time rate of Young's fringe shift.

Alternatively, the two delta function sources (the illuminated indents from the hardness tester) yield a cosine field distribution in the far field, i.e., a Fourier relationship exists between source and field distributions.[21] A second (two-dimensional) Fourier transform

LASER SPECKLE

Laser speckle is an interference phenomenon observed when a coherent source of electromagnetic radiation is reflected from a surface that is rough compared with the wavelength. It creates a speckled or wormy appearance. The term is somewhat misleading because the phenomenon is observed in a variety of situations such as synthetic aperture radar imagery. Shown in the figure (top) is a way of observing so-called "objective" or nonimaged speckle. A rough object is illuminated with a laser source, and the resulting scattered radiation is observed with a camera *without a lens*. Also shown (bottom) is the resulting pattern as displayed on a TV monitor. The sizes of the speckles are a function of the wavelength and observation geometry, and can be described quantitatively using Young's fringe analogy (see the boxed insert, Young's Fringes).

Subjective speckle is observed when the illuminated object is imaged (by the eye, a camera, film, etc.). In this case the image of the object appears mottled or speckled.

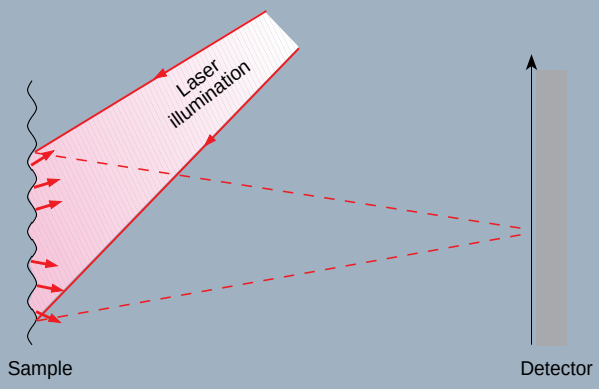

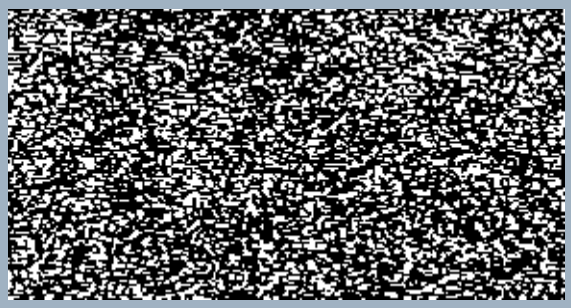

Laser speckle pattern.

(computed on the measured intensity) inverts this relationship, thus reproducing three delta functions. Because of the detection process, the focused line is not an image of the illumination stripe, but rather its autocorrelation.[22] For this simple case, therefore, we observe a pair of bright spots off axis and a third bright spot at DC.

In the objective speckle technique, the complex speckle pattern can be viewed as arising from all possible scatter pairs on the rough surface. Thus, each point in the focused speckle history corresponds to a unique scatterer separation on the object.

If the object under stress is straining equally at all scale sizes, the bright line in the frequency domain will be straight; however, without equal straining over the region of illumination,[17] the focused line will display curvature. The amount of curvature reflects the scale size dependence of strain.

The specific parameters used for our measurements are listed below, and results are summarized in Table 1. The test specimen was a 16-cm-long, 260-μm-dia. titanium wire undergoing a sawtooth variation in strain at a frequency of 7.5 mHz. Amplitudes of the stress waveforms were varied between two experiments.

Wavelength, 821 nm
Laser power, 70 mW
Source radius of curvature, ∞
Source incidence angles, $\pm 45°$
Observation distance, 0.52 m
Illuminated stripe (gauge length), 2 cm
Observation angle, 0°
Camera integration time, 350 and 500 ms
Camera sample interval, 0.5 and 1.0 s

The stress waveform for the first experiment is shown in Fig. 8 and the corresponding speckle histories in Fig. 9. By following previously developed procedures[17,18] using an FFT/autoregressive transformation (20 records, 3 poles), we estimated strain rates of 1.995 $\mu\epsilon$/s ($\pm$0.018 $\mu\epsilon$/s) in one experiment and 0.827 $\mu\epsilon$/s ($\pm$0.015 $\mu\epsilon$/s) in the other. Numbers in

Table 1. Experimental results.

Parameter	Experiment 1	Experiment 2
PZT velocity (μm/s)	0.3804	0.1406
Load rate (g/s)	1.144	0.7056
Strain rate from load cell ($\mu\epsilon$/s)[a]	1.863	0.7056
Strain rate from PZT ($\mu\epsilon$/s)	2.378	0.8785
Strain rate from speckle ($\mu\epsilon$/s)[a]	1.995, $\pm$0.018	0.827, $\pm$0.015
E estimated from speckle (GPa)	106	94.3
Differential speckle motion (pixels)	2.7	0.57

[a]Assuming Young's modulus E = 110.3 GPa.

YOUNG'S FRINGES

To elucidate the objective speckle technique, we use a particularly simple geometry, illustrated in the figure. Here we show a pair of scatterers separated by a distance s, illuminated with a plane wave at angle θ_s, and observed normally at a distance L_0. Although not necessary, for simplicity we ignore all rigid body motions. The intensity pattern in the observation plane is given by

$$I(x) \propto 2 + 2\cos[k(R_2 - R_1 + s\sin\theta_s)], \tag{1}$$

where k is the wavenumber $(2\pi/\lambda)$. From the figure, we have the following definitions for the geometric variables:

$$\begin{aligned} R_2 &= \sqrt{L_0^2 + (x + s/2)^2}\,, \\ R_1 &= \sqrt{L_0^2 + (x - s/2)^2}\,. \end{aligned} \tag{2}$$

With these definitions, Eq. 1 above becomes in the paraxial approximation

$$I(x) \propto 2 + 2\cos\left[\frac{2\pi s}{\lambda L_0}(x + L_0\sin\theta_s)\right]. \tag{3}$$

To quantify the behavior of this fringe pattern as the separation between the scatterers changes, we wish to keep track of a position of constant amplitude,

$$\frac{2\pi s}{\lambda L_0}(x + L_0\sin\theta_s) = C\,. \tag{4}$$

For small changes in separation δs, and the corresponding shift in the reference position δx, Eq. 4 yields

$$\left.\frac{\delta x}{\delta s}\right|_{x=0} = -L_0\epsilon_{xx}\sin\theta\,, \tag{5}$$

where the strain is defined as the fractional change in the scatterer separation. For a differential viewing geometry, the differential Young's fringe shift is

$$\delta A_x = \delta x(\theta_s) - \delta x(-\theta_s) = -2L_0\epsilon_{xx}\sin\theta_s\,. \tag{6}$$

With the procedure illustrated above, the formal results attributable to Yamaguchi[14] can be derived heuristically.

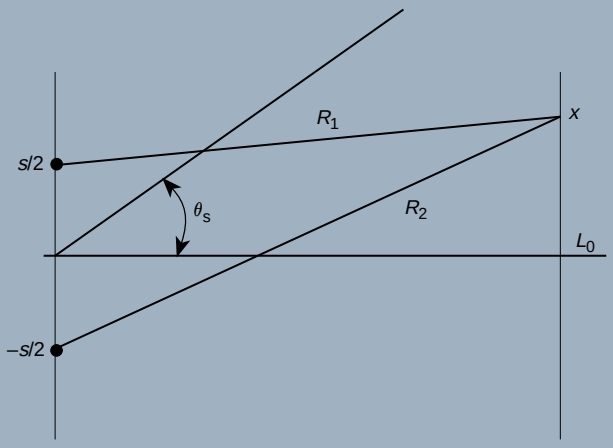

Geometry for point scatter pair.

parentheses represent 90% confidence intervals. Estimates of the strain rates obtained from the load cell data, assuming a Young's modulus of 110.3 GPa,[23] were 1.860 and 0.706 $\mu\epsilon$/s, respectively.

By using knowledge of the loading rates, along with our strain rate estimates, we were able to estimate the Young's modulus of the titanium fibers at 106.0 and 94.3 GPa, respectively. These figures are a bit low for bulk titanium but may be reasonable for fibers of this size.

How precisely can this approach estimate strain (or creep) rates? Several factors must be considered. Some are affected by the physical measurement approach and others by the subsequent data processing algorithm. Using a detailed error analysis,[24] it appears that the strain resolution is not imposed by the algorithm itself, but rather by a number of competing noise sources, which produce small, very-low-frequency transients. These include, but are not restricted to, laser wavelength drift; temperature transients in the support structure for the camera, laser, and tensile machine; barometric pressure fluctuations; deviations from symmetry for the two illumination directions; creep in the test fiber; and slippage of the fiber in collet chucks.

To the extent that these parameters are known or can be controlled, it appears that the algorithm that we have developed can accurately measure total strains on the order of 1 ppm.[24]

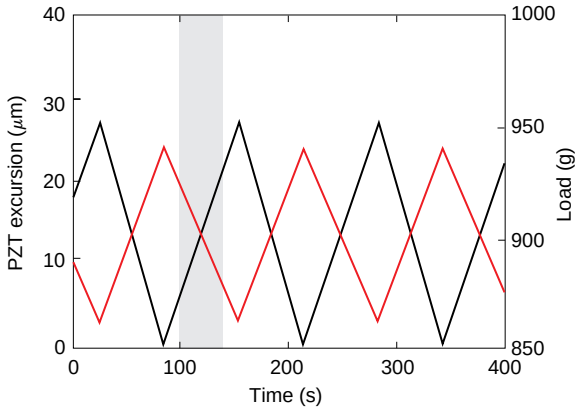

Figure 8. Stress waveform for first experiment (PZT = piezoelectric transducer, black curve; load cell, red curve; shaded area indicates data for which strain is estimated).

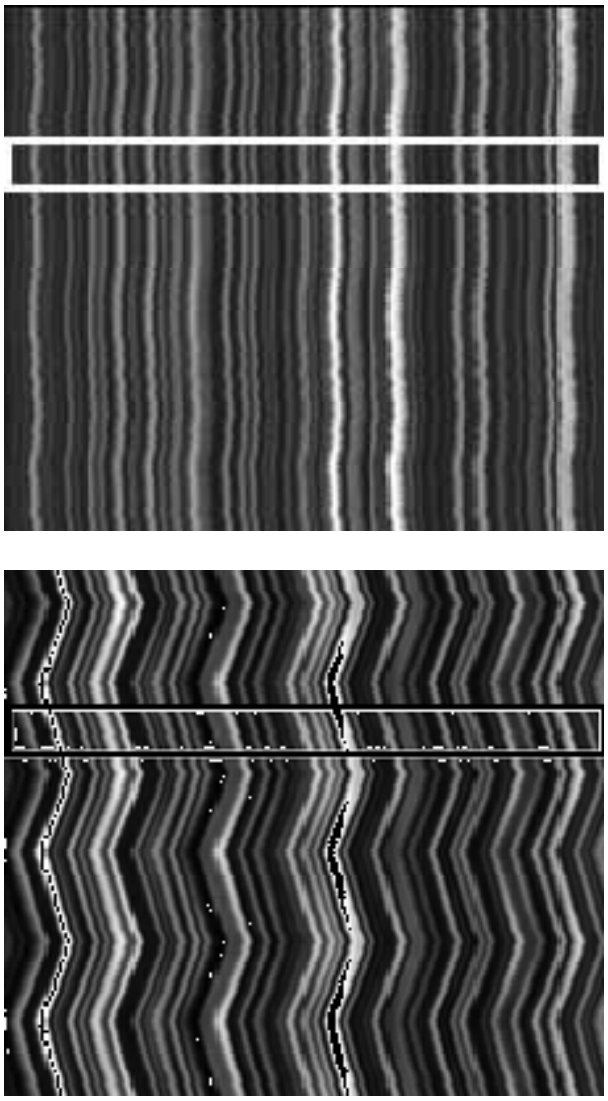

Figure 9. Speckle histories for each of the two illumination directions for the first experiment. Data for which strain estimates were made are boxed.

NOVEL SMART MATERIALS AND STRUCTURES MADE WITH ELECTRORHEOLOGICAL FLUIDS

Although the tasks described thus far were closely related, other tasks in the Advanced Materials Technology Insertion project allowed APL to keep its investment diversified and encouraged further collaborations across the Laboratory. The task described in this section concerns "smart" materials and structures, whose properties may be controlled in real time in response to their environment. Several applications were investigated, including control of optical signatures.[25] Another application was protection against shocks and vibrations over a wider range of conditions than is now possible. This task resulted in the fabrication of two promising smart structures for shock and vibration protection. The first, a composite plate whose vibrational modes and frequencies are controllable in real time, is described in Ref. 26. The second, a shock absorber with variable set point, is described here.

Our approach was based on electrorheological (ER) fluids, which have become the subject of increasing interest. An ER fluid is a dispersion of polarizable, dielectric particles in an electrically nonconducting liquid with a different dielectric constant. The rheological properties of the fluid, especially the yield stress and apparent viscosity, are then controlled by the application of a strong electric field (either DC or AC), at which time the particles line up in strings parallel to the field. The characteristics of the ER fluid differ according to (1) compounds selected, (2) particle size, concentration, and density, (3) additives to the basic fluid, (4) stabilizers and enhancers, (5) electrical conductivity of the fluid, and (6) electric field strength. ER effects are reversed upon removal of the field. Fluids prepared for AC applications seem more stable and perform better. Although the mechanism of the ER phenomenon is uncertain, the boxed insert (Rheology Model) provides a simplified discussion of ER behavior. A guide to ER applications is presented in Ref. 27, which compares ER fluids with shape memory alloys, piezoelectric devices, magnetic fluids, and other potential components of new intelligent materials.

To determine the characteristics of ER fluids needed to design the variable shock absorber, a rheometer was built consisting of two concentric cylinders separated by a 1-mm gap (Fig. 10). A constant driving force, which can be set over a range of values, moves the inner cylinder up with respect to the outer cylinder. The rheometer is filled with the ER fluid, and high DC voltages are impressed across the cylinders. The force on the inner cylinder and its displacement are measured as a function of time at zero field and for constant electric field intensities. From these data, shear stress as a function of applied voltage and the shear strain rate are determined, and the viscosity of the fluid may be calculated.

Rheometer tests were conducted on a simple ER fluid, namely, a dispersion of diatomaceous earth in a perfluorocarbon fluid base. ER behavior was observed and shear stress measurements made. Their magnitudes, shown in Fig. 11, were small for the intended application. This and other results led to the following general conclusions:

1. The ER shear force per unit area (shear stress) generated is small compared with forces normally provided by mechanical devices. To utilize this effect, an ER-based mechanical device should have a large area, operate over a long period of time (e.g., a vibration damper), or use a force multiplier device. An example of this kind of device is one that uses an ER fluid to control the area of the orifice of a shock absorber.

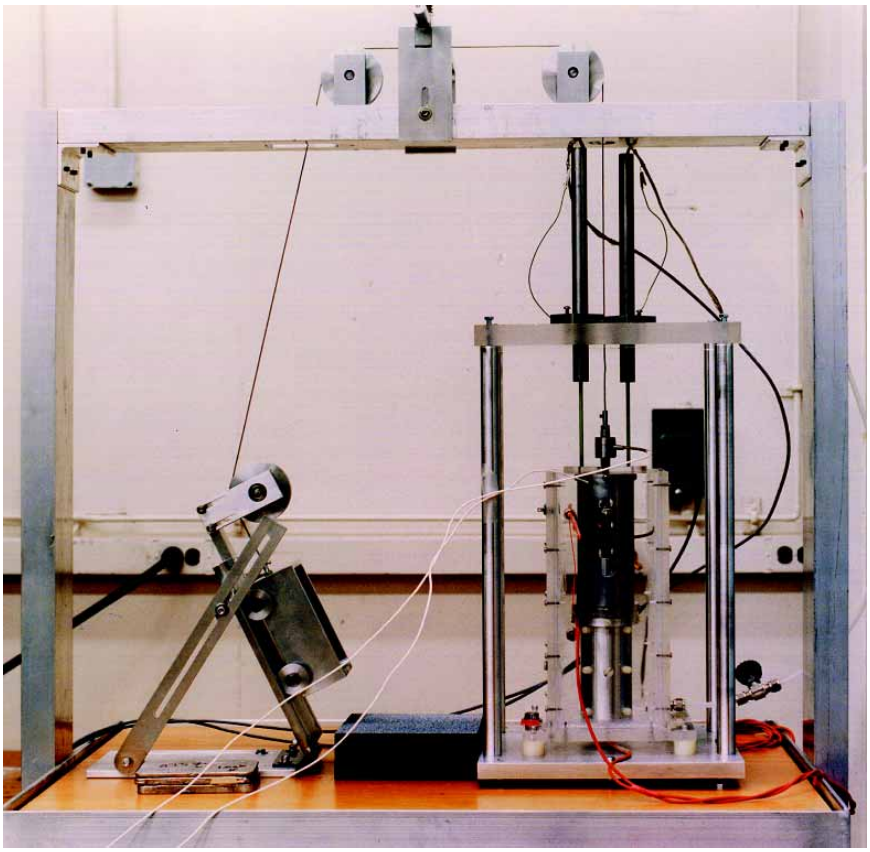

Figure 10. Rheometer for measuring the shear force exerted by electrorheological fluids.

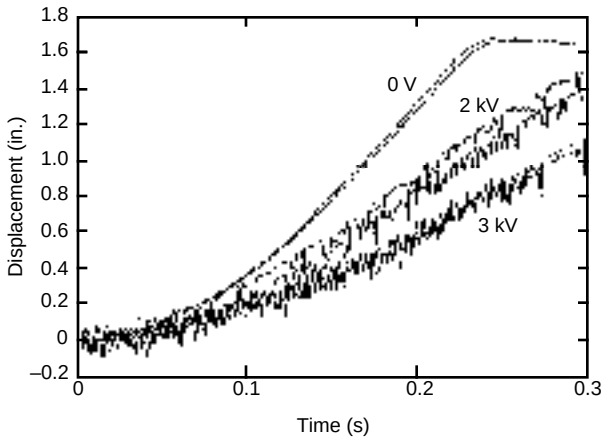

Figure 11. Effect of electric field on rheometer motion.

2. The electric field intensity required to provide a significant ER effect is about 3 kV/mm. At these intensities it is difficult to prevent arcing over a small gap. The electric interference noise produced by intermittent "micro" arcs somewhat degrades the outputs of the force and displacement transducers.
3. The most effective fluids are suspensions, but these are abrasive to moving parts and seals. ER devices should be designed to minimize this problem.

The design of the shock absorber reflects the lessons learned in the rheometer tests. The design concept, instead of relying directly on ER fluid effects for shock absorption, applies a conventional hydraulic fluid contained in a thick-walled cylindrical body. This fluid, driven through a variable-area orifice by a piston, provides the desired shock control. The area is varied by a sliding gate valve coupled to the moving piston shaft through an independent ER-controlled device. The device initiates the active damping required when a sensor system detects that a given set-level of shock impulse is exceeded. Advantages of this approach are as follows:

- Only a small amount of expensive ER fluid is required.
- Problems connected with the abrasiveness and degradation of the fluid are minimized.
- Few or no design changes are required to switch over to an improved fluid.
- Coupling to the piston shaft is straightforward.
- Accommodation of the high-voltage supply is simple.
- The critical hydraulic fluid properties are well known and stable.

A prototype shock absorber was fabricated (Fig. 12) and then delivered to John Coulter at Lehigh University for performance evaluation, final design changes, and fault correction. A programmable tensile machine was used for three phases of testing: (1) validation of the concept with measurements of the operational characteristics, (2) design and fabrication of the ER coupling device, and (3) evaluation of the integrated system.

For Phase 1, the gate valve was activated manually, the damper was subjected to representative forces and accelerations, and damper performance was determined. Data obtained were used for the controller design of Phase 2. Initial results showed the maximum damper forces attained to be of the order of 3000 lb when the orifice was closed and about 200 lb when open. Figures 13 and 14 give a representative force versus time plot and peak force versus frequency plot, respectively. The force required for control was found to be small, only about 10 lb. The concept is considered proved because the device operated well and did not leak. On the basis of information obtained, an ER clutch was designed and built. Phase 3, the task of testing the complete system, is now under way.

Thus, the shock damper design uses a very small volume of ER fluid to minimize abrasion. The working fluid is an inexpensive, conventional hydraulic fluid whose characteristics are uniform and well defined. Simple, unique devices can be based on this concept. Validation of the proof-of-principle of the shock damper shows that practical applications of this device, both military and civilian, are possible.

NONMETALLIC ELECTRIC MOTOR LINER MATERIALS

This task took the Advanced Materials Technology Insertion project in yet another direction, making important contributions toward the development of new materials that enhance submersible electric motors. The Navy needs such motors to drive submerged pumps, off-hull shipboard equipment such as trailing antennae and sonar line arrays, and underwater vehicle thrusters. New Navy initiatives use magnetic bearings in some underwater applications because they can be quieter than mechanical bearings and their controllers can actively cancel periodic noise sources.

There is also a commercial need to seal motors used in corrosive or toxic environments. Pumps with attached submersible motors can operate while entirely enclosed within their piping systems, so that no fluid leakage occurs at packing glands or wearing rings. Recently enacted legal restrictions on leakage and environmental emissions will increase the demand for these pumps and the materials that keep them totally sealed.

The key to submersible electric motors is the motor liner; specifically, the inner bore of radial flux submersible motors and magnetic bearings with wound stators must be sealed to prevent fluid from entering the windings. Metallic liners, often used in submersible motors, are waterproof but impose an eddy current loss. The loss can be a large proportion of the total motor energy. In one recent example, the eddy current losses in a 50-hp motor increased the total input power required by more than 10 hp. The loss is proportional to the thickness of the metal liner, the strength of the magnetic field across the gap, and the machine's rotational speed. It is inversely proportional to the resistivity of the liner material. For motor efficiency, especially in induction motors, liners must be thin to keep the "air gap" small.

Thus, the goals of this task were to identify appropriate materials for use as submersible motor liners and to develop processes for applying those materials to the inner bores of test motors. The materials were to be of low resistivity and thin to minimize the increase in the gap between static and rotating parts. The materials and processes were to be characterized on the basis of their ability to keep moisture out of the motor windings for long periods of time. The ideal material would have

RHEOLOGY MODEL

The figure presents stress–strain relationships typical of electrorheological (ER) fluids. Shear stress τ is plotted against shear strain γ and shear strain rate $\dot{\gamma}$ for given electric field intensities ξ. In these plots viscoelastic properties are exhibited. An important parameter is the static yield stress $\tau_{y,s}$, which is required to initiate flow in the presence of an electric field. Until this stress is exceeded, the material acts as an elastic solid under shear (the preyield region). It is a characteristic of the fluid regardless of any flow model representation. In the postyield region (the transition boundary defined by the γ_{critical} shear strain value), the material becomes a viscous fluid. Stress magnitudes strongly depend on the electric field intensity. Note that at zero field, shear stress is low and the fluid is of the Newtonian type.

No model completely describes the observed behavior of all ER materials. However, for most cases, the following equation describing the Bingham plastic model is sufficiently accurate for design work:

$$\tau(\dot{\gamma}, \xi) = \tau(\xi) + \eta\dot{\gamma}.$$

In this equation, the electric field–induced yield stress $\tau(\xi)$ is further approximated by the dynamic yield stress $\tau_{y,d}$, which is the zero strain rate intercept of the linear fit to the $\tau(\gamma)$ data, curve B. The plastic viscosity η is the slope of this fit. Observations show that static yield stresses are higher than dynamic stresses, as curve A indicates. After flow begins, curve B is followed as shear strain rate is increased. Then with decreasing strain rate, stresses fall along curve B and tend toward the dynamic yield stress intercept, characteristic of the fluid described by the Bingham model. (The interested reader is referred to Ref. 28 for a review of this topic.)

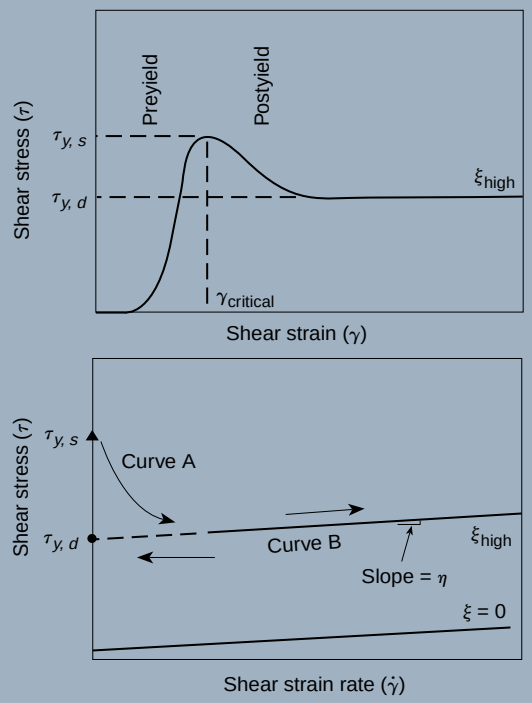

Shear stress versus shear strain and shear strain rate for a typical ER fluid.

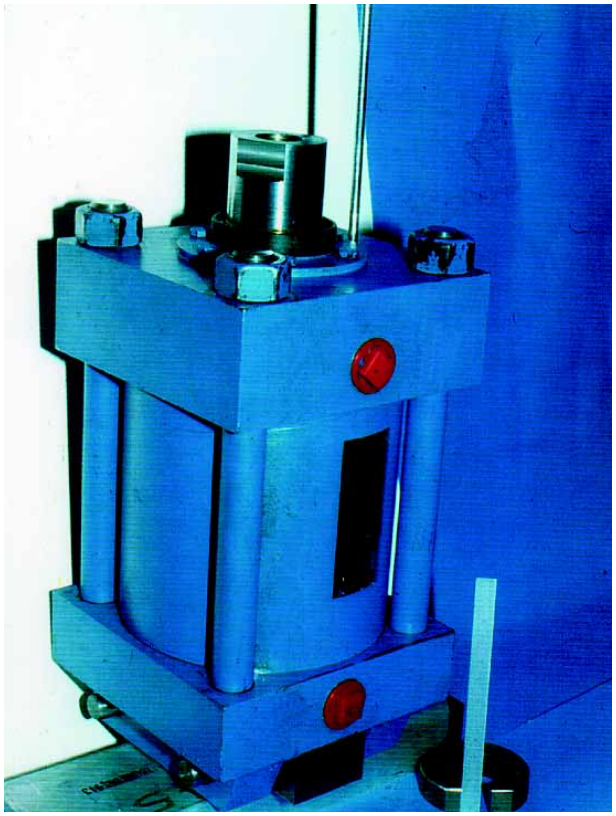

Figure 12. Electrorheological (ER) fluid–controlled experimental shock damper tested at Lehigh University. The piston shaft diameter is 2 in. The orifice control rod, shown beside the piston, is activated by means of an ER device. A 6-in. scale is shown in the figure.

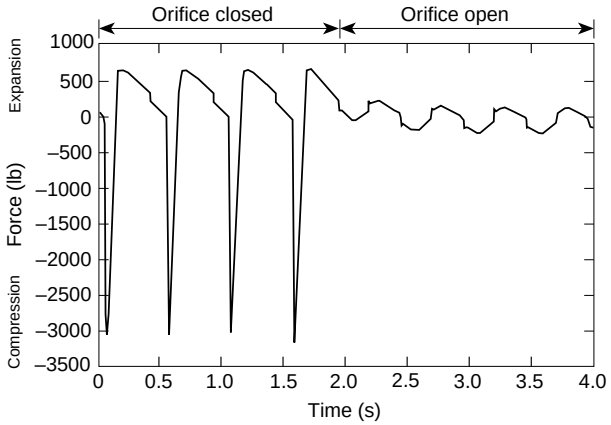

Figure 13. Force versus time at 2 Hz for a variable-orifice shock absorber.

infinite resistance to moisture penetration and zero thickness. In practical terms, the thickness of the material would be small relative to the diameter of the motor rotor.

A mylar film sandwiched between two thicknesses of polyester fabric was examined as an initial candidate sealing material. The sample obtained was 0.015 in. thick and would have met the criterion for being thin relative to the bore diameter of most motors. But

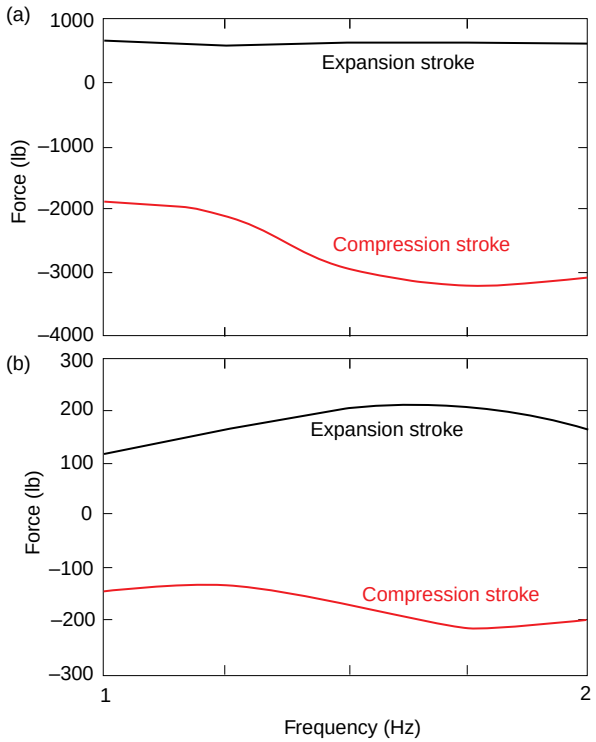

Figure 14. Measured performance of the prototype shock damper. Peak forces are plotted versus frequency: (a) orifice closed, (b) orifice open.

attempts to develop the process for attaching this material to the motor internals showed that the splice needed at the cylinder's longitudinal seam could not be made without excessive increases in the thickness at the seam location. An ineffective splice would allow moisture penetration into the sensitive steel parts of the motor core.

A second material attempted was preimpregnated glass-reinforced plastic. It was possible to construct a continuous cylinder of this material without cross-sectional irregularities. The cylinder was constructed by applying a rectangular sheet of the uncured/cured material to a cylindrical mandrel and wrapping it with heat shrink tape. Heat from the curing cycle shrank the tape, forcing resin to flow into the longitudinal splice and causing some intertwining of the fibers there.

This initial attempt to manufacture a thin-walled hollow cylinder provided insight into some process difficulties. Resin shrinks as it cures. With the very thin section of material on the mandrel, the shrinkage could cause enough tensile stress to fracture the part. In initial attempts, the part failed at its weakest section (the longitudinal seam), but we subsequently found that the shrinkage problem could be controlled by careful attention to cure rate.

To test the cylinder's ability to prevent moisture penetration, it was installed in the inner bore of a small, inexpensive electric fan motor. The motor had an enclosed case and was designed for heat conduction

through its exterior. The motor case made it easy to encapsulate the motor winding sections not protected by the thin cylindrical liner. The encapsulant was a polyurethane similar to the type used in submarine cables.

The motor used inexpensive sleeve bearings. Since it was never intended to run under water, it was vulnerable to corrosion and bearing failure. For the initial underwater test, the investigators coated the parts with epoxy paint and filled the bearing cavities with water-resistant grease. The small motor was run under water in a laboratory container for the first test.

The test had two significant results. First, the encapsulated motor, when run in air, was no hotter than an identical motor in the original condition. This finding gave investigators confidence in their initial assumption that the encapsulant and liner materials would not change the heat-carrying capabilities of this particular motor. Second, high potential insulation checks of the motor showed that the thin plastic liner did not prevent moisture penetration. In the original dry condition, an induction motor's insulation should provide a resistance of at least 2000 MW between winding and case. Most have significantly more. A perfectly sealed submersible motor should have similar characteristics. A good measure of moisture penetration into the motor is its insulation resistance. After the first 60 h of running submerged, the motor's measured resistance was only 1 MW. This indicated excessive moisture encroachment, and the test was abandoned.

A third material consisted of a sandwich of two very thin sheets of glass-reinforced plastic with a thin foil of metal between them. The metal foil was 0.003 in. thick, and the total thickness of the sandwich was 0.015 in. A new cylindrical shell of the sandwich material was installed on the center bore of an electric motor identical to the one used for the first test (Fig. 15). After 1969 h of running under water and 289 h under water deenergized, the motor still had an insulation resistance of 12,000 MW. The liner material for which the test was intended appeared to be successful. After its long underwater endurance, this small, inexpensive motor was very corroded but still functional.

With the success of the liner material on a small motor, a special apparatus (Fig. 16) was developed for testing much larger (0.5-hp) submersible motors in a continuously cooled water container. The motor selected had stainless steel corrosion-resistant parts and sealed bearings. Although "splashproof," it is not intended for submerged operation because its windings are not protected at its inner bore. After this motor was treated with the new material and processes from the initial efforts, it showed no degradation in extended underwater tests.

Figure 15. This inexpensive motor with badly corroded exterior remains operable and safe after 2258 h under water.

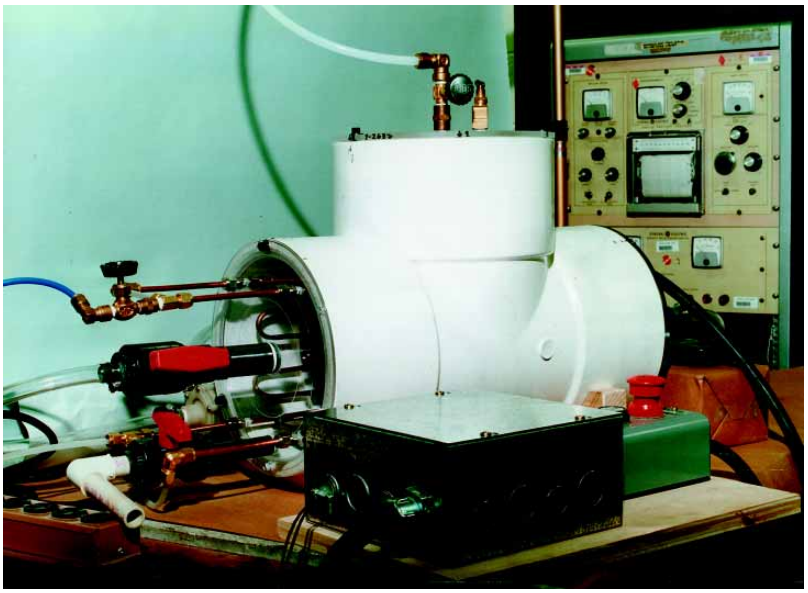

Figure 16. This specially constructed test cell can change and monitor pressure and temperature during tests.

CONCLUSION

The Advanced Materials Technology Insertion project comprised eight different tasks, which enhanced the Laboratory's technical and business position in the field of advanced structural materials. In addition, beneficial collaborations were established among staff members in different departments of APL and with the Homewood campus of the University. The project witnessed a growth in materials activities at the Laboratory—notably in the Aeronautics Department, the Technical Services Department, and the Research Center—and kept alive an awareness of the importance of advanced structural materials to APL.

REFERENCES

1 Billig, F. S., "Tactical Missile Design Concepts," *Johns Hopkins APL Tech. Dig.* **4**(3), 139 (1983).
2 Newman, R. W., "Oxidation-Resistant High-Temperature Materials," *Johns Hopkins APL Tech. Dig.* **14**(1), 24–28 (1993).
3 Bargeron, C. B., Benson, R. C., Newman, R. W., Jette, A. N., and Phillips, T. E., "Oxidation Mechanisms of Hafnium Carbide and Hafnium Diboride in the Temperature Range 1400 to 2100°C, *Johns Hopkins APL Tech. Dig.* **14**(1), 29–35 (1993).
4 Hunter, L. W., "High-Temperature Chemistry of Materials: An Update," *Johns Hopkins APL Tech. Dig.* **11**(1–2), 168–174 (1990).
5 Hunter, L. W., "High-Temperature Chemistry of Materials," *Johns Hopkins APL Tech. Dig.* **7**, 362–371 (1986).
6 Hunter, L. W., Kuttler, J. R., Bargeron, C. B., and Benson, R. C., "Oxidation of Refractory Carbides," in *Proc. 10th Annual Conf. on Composites and Advanced Ceramic Materials*, Cocoa Beach, FL (1986).
7 Hunter, L. W., and Duncan, D. D., "Improved Control of Oxidation and Mechanical Tests at Ultra-High Temperatures," in *Proc. 16th Annual Conf. on Composites, Materials, and Structures*, Cocoa Beach, FL (12–15 Jan 1992).
8 Wajer, S. D., and Wilson, D. E., *Microanalysis of Hafnium Carbide Using Scanning Electron Microscopy (SEM) and Energy Dispersive Spectroscopy (EDS)*, JHU/APL TEQ/SDW-92-134 (27 Apr 1992).
9 Kuttler, J. R., and Friedman, M. A., *Oxidation of Hafnium Carbide: Constant Thermal Conductivity*, JHU/APL AM-90-P046 (1 Mar 1990).
10 Kuttler, J. R., *Oxidation of Hafnium Carbide: Variable Thermal Conductivity*, JHU/APL AM-90-P061 (3 Apr 1990).
11 Kuttler, J. R., *Oxidation of Hafnium Carbide: General Surface Boundary Conditions*, JHU/APL AM-90-P082 (31 Jul 1990).
12 Friedman, M. A., *Oxidation of Hafnium Carbide. Calculation of Effect of Temperature Gradient*, JHU/APL AM-90-P140 (3 Jul 1990).
13 Hunter, L. W., and Kuttler, J. R., "The Enthalpy Method for Ablation-Type Moving Boundary Problems," *J. Thermophys. Heat Trans.* **5**, 240–242 (1991).
14 Yamaguchi, I., "Advances in the Laser Speckle Strain Gauge," *Opt. Eng.* **27**(3), 214–218 (1988).
15 Barranger, J. P., *Two-Dimensional Surface Strain Measurement Based on a Variation of Yamaguchi's Laser-Speckle Strain Gauge*, NASA Technical Memorandum 103162, NASA Lewis Research Center, Clevelend, OH (1990).
16 Takemori, T., Fujita, K., and Yamaguchi, I., "Resolution Improvement in Speckle Displacement and Strain Sensor by Correlation Interpolation, in *Laser Interferometry IV; Computer-Aided Interferometry, Proc. SPIE* **1553**, pp. 137–148 (1991).
17 Duncan, D. D., Kirkpatrick, S. J., Mark, F. F., and Hunter, L. W., "Transform Method of Processing for Speckle Strain Rate Measurements," *Appl. Opt.* **33**(22), 5177–5186 (1994).
18 Duncan, D. D., Mark, F. F., and Hunter, L. W., "A New Speckle Technique for Noncontact Measurement of Small Creep Rates," *Opt. Eng.* **31**(7), 1583–1589 (1992).
19 Marple, S. L., *Digital Spectral Analysis with Applications*, Prentice-Hall, Englewood Cliffs, NJ (1987).
20 Sharpe, W. N., "Applications of the Interferometric Strain/Displacement Gauge," *Opt. Eng.* **21**(3), 483–488 (1982).
21 Goodman, J. W., *Statistical Optics*, John Wiley & Sons, New York (1985).
22 Goodman, J. W., "Statistical Properties of Laser Speckle Patterns," in *Laser Speckle and Related Phenomena*, J. C. Dainty (ed.), Springer-Verlag, Berlin (1975).
23 McClintock, F. A., and Argon, A. S., *Mechanical Behavior of Materials*, Addison-Wesley, Reading, MA (1966).
24 Duncan, D. D., Kirkpatrick, S. J., Mark, F. F., and Hunter, L. W., "Measurement of Strain Rates in Reinforcement Fibers," *Meas. Sci. Technol.* (accepted) (1995).
25 Hunter, L. W., Mark, F. F., Kitchin, D. A., Feinstein, M. R., Blum, N. A., et al., "Optical Effects of Electro-Rheological Fluids," *J. Intell. Mat. Syst. Struct.* **4**, 415–418 (1993).
26 Coulter, J. P., Don, D. L., Yalcintas, M., and Biermann, P. J., "An Experimental Investigation of Electro-rheological Material Based Adaptive Plates," in *Proc. ASME Winter Annual Meeting*, Chicago (6–11 Nov 1994).
27 Mark, F. F., *Compilation of Adaptive/Smart Material Characteristics*, JHU/APL AM-94-S005 (6 Jun 1994).
28 Block, H., and Kelly, J. P., "Review Article, Electrorheology," *J. Phys. D: Appl. Phys.* **21,** 1661–1677 (1988).

ACKNOWLEDGMENT: The Advanced Materials Technology Insertion project was supported by independent research and development funds. The charter, objectives, and long-term strategic plans of the project were developed by Lawrence W. Hunter, Richard P. Suess, Frank G. Arcella, Paul J. Biermann, John R. Coleman, and Joseph J. Suter.

THE AUTHORS

LAWRENCE W. HUNTER is a member of APL's Principal Professional Staff. He holds a B.Sc. (hons.), first class, in chemistry (Carleton University, Ottawa, Canada, 1967) and a Ph.D. in theoretical chemistry (University of Wisconsin, Madison, 1972). He has been employed at APL since 1973 and has worked on many different interesting projects, typically related to combustion, missile systems, and the F/A-18. Dr. Hunter coordinated two APL independent research and development (IR&D) thrust areas and currently helps coordinate Aeronautics Department IR&D activities. He has contributed to over 80 refereed publications including one listed in "The Twenty-Two Most Frequently Cited APL Publications," *John Hopkins APL Tech. Dig.* **7**(2), 221–232 (1986). His e-mail address is Lawrence.Hunter@jhuapl.edu.

DONALD D. DUNCAN is Supervisor of the Measurements and Propagation Section of APL's Electro-Optical Systems Group. He received his Ph.D. in electrical engineering from The Ohio State University in 1977. From 1977 to 1983, he was employed by Pacific-Sierra Research Corporation, where he modeled optical propagation phenomena such as aerosol scatter, atmospheric turbulence, and high-energy laser effects (e.g., thermal blooming, aerosol burnoff). Since joining APL in 1983, Dr. Duncan has worked on various biomedical engineering projects; provided test program support and data analysis for a tracking/guidance synthetic aperture radar system; and worked on many measurement, modeling, and diagnostic equipment projects in support of the hypersonic interceptor. He also teaches courses in Fourier and statistical optics at The Johns Hopkins University G.W.C. Whiting School of Engineering. His e-mail address is Donald.Duncan@jhuapl.edu.

FRANK F. MARK studied physics at the Massachusetts Institute of Technology and was a member of the Advanced Systems Group of APL's Aeronautics Department. His work focused on fluid dynamics, biomedical research, optics, and advanced materials. Mr. Mark is now retired.

JAMES S. O'CONNOR is a member of the APL Principal Professional Staff. He has a B.M.E. (mechanical engineering) from the University of Detroit (1966) and an M.Sc. (aerospace engineering) from Ohio State University (1968). Employed at the Laboratory since 1968, Mr. O'Connor has participated in the mechanical design of guided missile systems, spacecraft, automated transportation systems, and the Ocean Thermal Energy Conversion power plant. His e-mail address is James.O'Connor@jhuapl.edu.

JAMES W. WHITE received a B.S. in engineering physics from the University of Oklahoma in 1972. In 1980, the Massachusetts Institute of Technology awarded him an M.S. in mechanical engineering and the Professional Degree of Ocean Engineer. After completing his career as a naval officer and working in private industry for several years, Mr. White joined APL in 1993. He is a member of the Aeronautics Department working in F/A-18 supplier management. Mr. White is the inventor of an advanced pump, now undergoing Navy testing, that uses a submerged motor drive. His e-mail address is James.White@jhuapl.edu.